Bulletin of the Seismological Society of America, Vol. 103, No. 6, pp. 3073–3082, December 2013, doi: 10.1785/0120130101

Combination of Hi-net and KiK-net Data for Deconvolution Interferometry

by Nori Nakata*

Abstract Application of deconvolution interferometry to wavefields observed by KiK-net, a strong-motion recording network in Japan, is useful for estimating wave velocities and *S*-wave splitting in the near surface. At the location of the borehole accelerometer of each KiK-net station, a velocity sensor is also installed as a part of a high-sensitivity seismograph network (Hi-net). I present a technique that uses both Hi-net and KiK-net records for computing deconvolution interferometry. The deconvolved waveform obtained from the combination of Hi-net and KiK-net data is similar to the waveform computed from KiK-net data only. This similarity in the waveforms indicates that one can use Hi-net wavefields for deconvolution interferometry. Because Hi-net records have a high signal-to-noise ratio (SNR) and high dynamic resolution, SNR and quality of amplitude and phase of deconvolved waveforms can be improved with Hi-net data. These advantages are especially important for short-time moving-window seismic interferometry and deconvolution interferometry using coda waves.

Introduction

Data from a strong-motion recording network, KiK-net, have been used for estimating near-surface properties by computing spectral ratios and seismic interferometry based on deconvolution (e.g., Sawazaki *et al.*, 2006, 2009). KiK-net has been operated by the National Research Institute for Earth Science and Disaster Prevention (NIED) since 1996 (Aoi *et al.*, 2004, 2011); therefore, these data are useful for time-lapse studies. KiK-net includes about 700 stations distributed all over Japan, and each station has two three-component accelerometers: one at the surface and the other in a borehole. The depth of the boreholes is mostly 100–210 m, and some boreholes are more than 1000 m deep.

Applying seismic interferometry to KiK-net records, Sawazaki *et al.* (2009) and Yamada *et al.* (2010) estimated velocity reduction after the 2000 western Tottori earthquake and the 2008 Iwate–Miyagi Nairiku earthquake, respectively. Nakata and Snieder (2012a) found that reductions in *S*-wave velocity after large earthquakes occurred in the Niigata prefecture in Japan, and Nakata and Snieder (2011) and Takagi and Okada (2012) discovered a reduction in *S*-wave velocity after the 2011 Tohoku-Oki earthquake. These reductions partly recover logarithmically with time (Nakata and Snieder, 2011, 2012b). Although Sawazaki and Snieder (2013) estimated *P*-wave velocities using this technique, computing *P*-wave velocities is more challenging than computing *S*-wave velocities because of the shallow depth of the boreholes. Wu and Peng (2011, 2012) found a reduction in peak frequencies of the spectral ratio and a recovery with time after the Tohoku-Oki earthquake. Nakata and Snieder (2012b), Takagi and Okada (2012), and Sawazaki and Snieder (2013) investigated time-lapse changes of shear-wave splitting due to the Tohoku-Oki earthquake, although their conclusions are different. One can also calculate the changes in *S*-wave velocities caused by precipitation with this technique (Nakata and Snieder, 2012a).

A high-sensitivity seismograph network, Hi-net, is also maintained by NIED to continuously record ground motion (Obara *et al.*, 2005). Hi-net velocity meters are located at the same position as the KiK-net borehole accelerometers. Hi-net records, especially ambient-noise data, are used for estimating changes in velocity in deeper zones (e.g., Wegler *et al.*, 2009; Minato *et al.*, 2012). Although KiK-net and Hi-net receivers are collocated, no study has yet used combinations of KiK-net and Hi-net data for the techniques of spectral ratio or seismic interferometry. Because KiK-net and Hi-net have different targets (specifications are summarized in Table 1 and Okada *et al.* [2004]), the properties of the observed records are different; briefly, KiK-net has the larger dynamic range, which prevents saturation of amplitudes for large earthquakes, and Hi-net has the higher sensitivity to record small ground motions. Clinton and Heaton (2002) found some advantages of using strong-motion velocity meters compared with using strong-motion accelerometers; we are able to reduce numerical error to estimate displacement

*Formerly at Center for Wave Phenomena, Colorado School of Mines, 1500 Illinois Street, Golden, Colorado 80401.

Table 1
Specifications of KiK-net and Hi-net Systems

	KiK-net	Hi-net
Sensor type	Accelerometer	Velocity meter
Sensor location	Surface and downhole	Downhole
Sensor component	Three components	Three components
Recording system	Event trigger	Continuous
Sampling ratio	100 Hz	100 Hz
Dynamic range	±2000 cm/s²*	≈0.2 cm [sensitivity ±2 V/(cm/s)]
A/D resolution	22 bit	27 bit
Dynamic resolution†	4.765×10^{-4} cm/s²*	1.023×10^{-5} cm/s

For further information, see Aoi *et al.* (2004, 2011) and Obara *et al.* (2005). Some parameters are only for FKSH12 and N.HTAH in 2012.
*Values are for downhole sensors.
†Dynamic resolution means resolution of amplitude.

because we need only one integration, and the signal-to-noise ratio (SNR) is better, especially for long periods.

Some velocity meters, which are not for strong-motion recording, have small dynamic ranges. The amplitudes of records of these velocity meters may saturate when large earthquakes occur. Although Hi-net receivers are not strong-motion velocity meters, the dynamic range of the Hi-net sensors is much wider than that of conventional velocity meters (Table 1). Therefore, we can use earthquake records observed by Hi-net when the earthquakes are relatively small. For large earthquakes, Shiomi *et al.* (2005) present criteria to detect amplitude saturation of Hi-net data (introduced later).

In this study, I propose a technique using both KiK-net and Hi-net data to improve the quality of correlograms obtained by deconvolution interferometry. I first compare observed records of Hi-net and KiK-net in the time and frequency domains. Then, I briefly introduce deconvolution interferometry and apply this interferometry to KiK-net and Hi-net data. Finally I compare deconvolved waveforms and present advantages of using both Hi-net and KiK-net data rather than only KiK-net records.

Comparison of Observed Waveforms of Hi-net and KiK-net

Figure 1 shows waveforms observed by Hi-net and KiK-net receivers at the same location in the Fukushima prefecture (Hi-net code, N.HTAH; KiK-net code, FKSH12). The waveforms in Figure 1a,e,f are the unfiltered ground motion in the north–south (NS) horizontal component recorded by Hi-net, KiK-net borehole, and KiK-net surface sensors, respectively. Because borehole receivers do not align to the exact NS direction due to a technical limitation, I first rotate Hi-net and KiK-net borehole records to the NS direction (Shiomi *et al.*, 2003). The amplitude of the waveform observed by the KiK-net surface accelerometer (Fig. 1f) is greater than twice as large as the amplitude of the KiK-net borehole record (Fig. 1e), which might be an indication of the site amplification (e.g., Héloïse *et al.*, 2012), and is beyond the scope of this study.

I integrate and differentiate the waveform shown in Figure 1a using Fourier transforms to compute displacement and acceleration waveforms, respectively (Fig. 1b,c). Theoretically, the waveform in Figure 1c is the same as that in Figure 1e because these waveforms are the records of the same earthquake at the same location. I compare the wavefields in Figure 1c and 1e in the frequency domain (Fig. 2). In the ideal case (where the waveform in Fig. 1c is the same as that in Fig. 1e), the amplitude ratio (the gray line in Fig. 2b) and the phase difference (the gray dots in Fig. 2c) are 1° and 0°, respectively. The main reason for deviation from the ideal case is the difference in the receiver responses of Hi-net and KiK-net. Hi-net and KiK-net receivers have flat responses between 1–30 Hz and DC-20 Hz, respectively (Okada *et al.*, 2004; Obara *et al.*, 2005). The reduced values of the gray line in Figure 2b below 1.5 Hz are caused by the nonflat response of the Hi-net sensor, and the large values above 20 Hz are due to the response of the KiK-net sensor.

Because I use the frequency range of 1–13 Hz for deconvolution interferometry (Nakata and Snieder, 2012a), I correct the receiver response of the Hi-net sensor. Because phase information is important for deconvolution interferometry, I apply a correction for the receiver response to both the amplitude and phase of the waveform in Figure 1a. I compute response-corrected acceleration waveforms as

$$H_a(t) = \int_{-\infty}^{\infty} H_a(\omega) e^{-i\omega t} d\omega = \int_{-\infty}^{\infty} \frac{(i\omega - p_0)(i\omega - p_1)}{i\omega - z_0} H_v(\omega) e^{-i\omega t} d\omega, \quad (1)$$

(Havskov and Ottemöller, 2010), in which $H_a(t)$ and $H_a(\omega)$ are the response-corrected acceleration waveforms in the time and frequency domains, respectively; $H_v(\omega)$ is the Hi-net observed record in the frequency domain after scaling by the dynamic resolution shown in Table 1; ω is the angular frequency; i is the imaginary unit; and $z_0 = 0.0 + 0.0i$, $p_0 = -4.398230 + 4.487092i$, and $p_1 = -4.398230 - 4.487092i$ are the complex zeros and poles of the Hi-net sensor. Here, the dynamic resolution means the resolution of amplitude in acceleration units (cm/s²) for KiK-net and in velocity units (cm/s) for Hi-net.

Figure 1d shows the response-corrected acceleration waveform computed from the Hi-net observed record (Fig. 1a). Although the time-domain waveforms in Figure 1c and 1d are almost the same based on a visual inspection, these wavefields are clearly different in the frequency domain (the dashed and solid black lines in Fig. 2a). The black symbols of Figure 2b and 2c illustrate the amplitude ratio and the phase difference between this response-corrected acceleration waveform and the KiK-net record. As shown in Figure 2, the amplitude ratio and phase difference after the correction are close to 1° and 0°, respectively, in a wider frequency range, compared with the

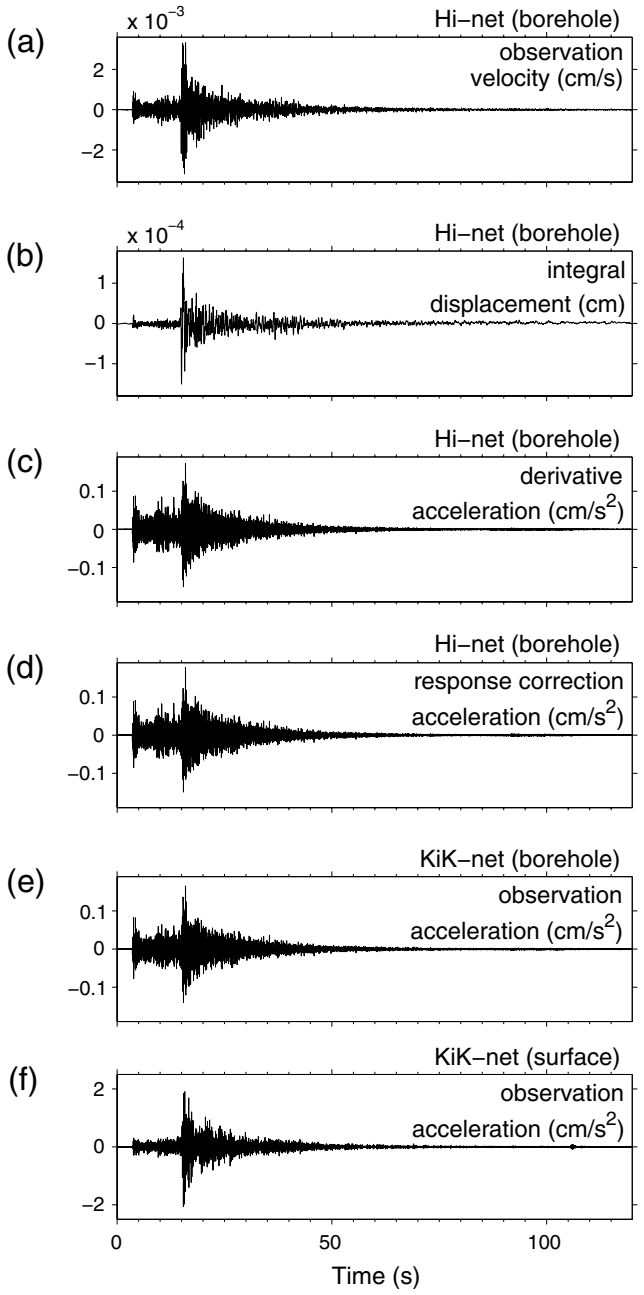

Figure 1. (a) Observed Hi-net waveform of one earthquake recorded in the NS horizontal component at N.HTAH (37.2139° N and 140.5736° E). This earthquake occurred at 18:17:59, 12 January 2012 (JST). The epicenter is at 37.595° N and 141.616° E, and the depth is 42.9 km. (b, c) Integral (displacement) and derivative (acceleration) of the waveform shown in panel (a). (d) Acceleration waveform computed from the waveform in panel (a) with the correction of the receiver response (equation 1). (e, f) Observed waveforms recorded by the collocated KiK-net accelerometers (FKSH12) in the borehole and at the surface. Units of each waveform are shown at right of each panel.

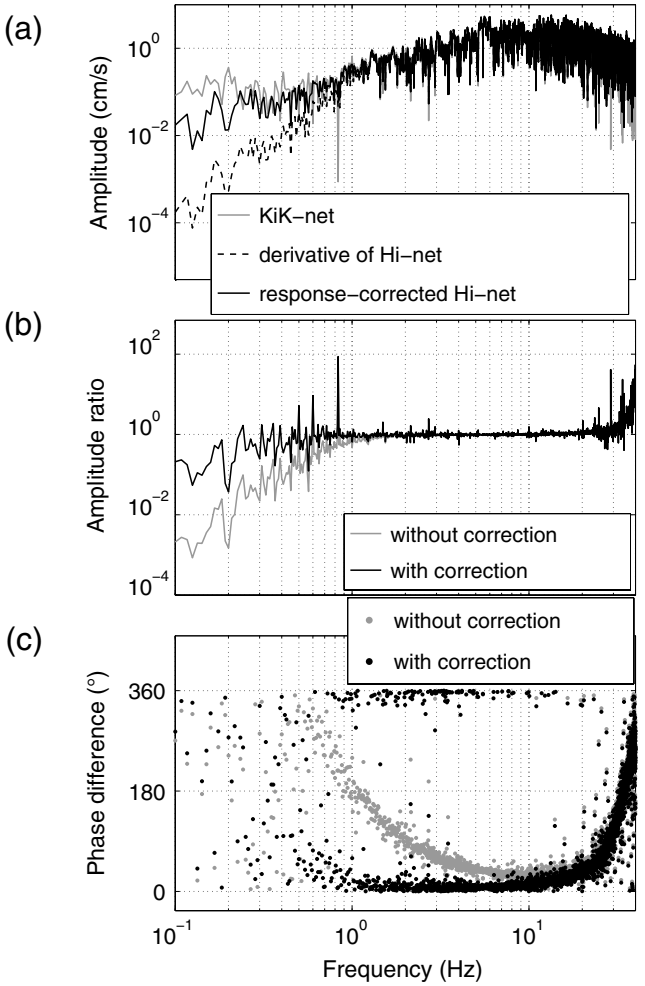

Figure 2. (a) Comparison of amplitude spectra computed from the waveforms in Figure 1c (dashed black line, derivative of Hi-net), Figure 1d (solid black line, response-corrected Hi-net), and Figure 1e (gray line, KiK-net). (b) Ratios of amplitude spectra (Hi-net/KiK-net). The gray line is computed from the amplitude spectra of the waveforms in Figure 1c and 1e (the ratio of the gray and dashed black lines in panel a), and the black line from Figure 1d and 1e (the ratio of the gray and solid black lines in panel a). (c) Differences of phase spectra (Hi-net–KiK-net). The gray and black dots are computed from the waveforms used for the gray and black lines in panel (b). Because of the display, some dots are shown around 360°.

ratio and difference without the correction. Note that because of this correction, I successfully improve the similarity of the waveforms of KiK-net and Hi-net in the frequency range used in this study (1–13 Hz). Therefore, I use the response-corrected acceleration waveform for deconvolution interferometry. More examples of the amplitude ratio and the phase difference using another earthquake and station are shown in Figures A1 and A2, which also show the improved similarity after correcting the receiver response.

Figure 3 shows the comparison of the waveforms shown in Figure 1d,e in three time intervals, which are before the *P*-wave arrival, at the maximum-amplitude waves, and at later coda waves. The KiK-net and Hi-net waveforms in Figure 3b are almost the same (correlation coefficient 0.96); those in Figure 3c are also similar, but some amplitudes are different (correlation coefficient 0.86). These similarities indicate that I can use Hi-net data as strong-motion records. In contrast,

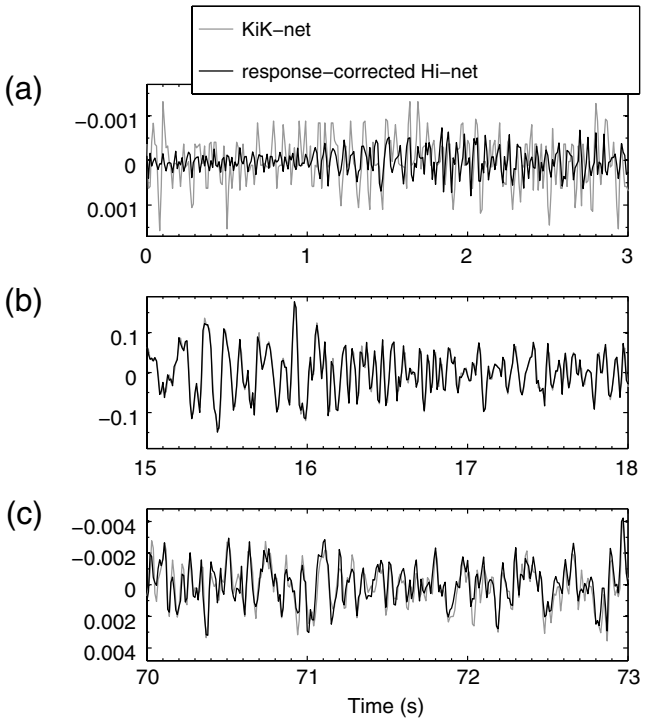

Figure 3. Comparison of the waveforms shown in Figure 1d (black line, Hi-net) and Figure 1e (gray line, KiK-net) at different time intervals. Note that the amplitude scales of each panel are different. The unit of the vertical axes is cm/s^2.

the Hi-net waveform in Figure 3a is significantly different from the KiK-net record. One reason of this discrepancy is caused by the difference of SNR in Hi-net and KiK-net as mentioned in Clinton and Heaton (2002). The other reason is the difference of the dynamic resolutions. Because the dynamic ranges and the analog-to-digital (A/D) converters of KiK-net and Hi-net receivers are different due to the difference of their targets, the dynamic resolutions for KiK-net and Hi-net systems are different (Table 1). In KiK-net records, the dynamic resolution is approximately 5×10^{-4} cm/s^2, which means that the KiK-net waveform in Figure 3a fluctuates over only one or two samples in amplitude. Note that the Hi-net system has the much higher dynamic resolution, and the resolution depends on the frequency (Obara *et al.*, 2005).

Although the Hi-net system has the higher SNR and the higher dynamic resolution, the dynamic range for the Hi-net system is smaller than that of the KiK-net system; therefore, the amplitude of Hi-net records can be saturated when a large earthquake occurs. I carefully examine to confirm that the records of the earthquakes used in this study are not saturated, but for dealing with large amounts of data, automatic methods for the examination are useful. Shiomi *et al.* (2005) propose several criteria to evaluate whether the amplitudes of Hi-net records are saturated or not. Based on Shiomi *et al.* (2005), when (1) the maximum amplitude of KiK-net borehole records is smaller than 3.95 cm/s^2 and (2) the maximum displacement computed by the integration of Hi-net records is smaller than 0.09 cm, the Hi-net waveform of the earthquake is not likely to be saturated. The Hi-net records used in this study are much smaller than these criteria (Fig. 1).

Deconvolution Interferometry Using Hi-net and KiK-net Data

Deconvolution Interferometry

Conventionally for deconvolution interferometry, one uses only KiK-net records (e.g., Nakata and Snieder, 2012a):

$$D_{KK}(S,B,t) = \int_{-\infty}^{\infty} \frac{K_a(S,\omega)}{K_a(B,\omega)} e^{-i\omega t} d\omega \approx \int_{-\infty}^{\infty} \frac{K_a(S,\omega) K_a^*(B,\omega)}{|K_a(B,\omega)|^2 + \epsilon \langle |K_a(B,\omega)|^2 \rangle} e^{-i\omega t} d\omega, \quad (2)$$

in which S and B are the locations of receivers at the free surface and in the borehole, K_a is the wavefield observed by a KiK-net accelerometer, the asterisk is the complex conjugate, $\langle \cdots \rangle$ is the average power spectrum, and ϵ is a regularization parameter to obtain stable deconvolved waveforms (Clayton and Wiggins, 1976). After the deconvolution interferometry, the borehole receiver behaves as a virtual source, and $D_{KK}(S,B,t)$ corresponds to the wavefield propagating from the virtual source to the surface receiver (Nakata and Snieder, 2012a). Here, I replace the wavefield in the denominator of equation (2) by Hi-net data:

$$D_{KH}(S,B,t) = \int_{-\infty}^{\infty} \frac{K_a(S,\omega)}{H_a(B,\omega)} e^{-i\omega t} d\omega \approx \int_{-\infty}^{\infty} \frac{K_a(S,\omega) H_a^*(B,\omega)}{|H_a(B,\omega)|^2 + \epsilon \langle |H_a(B,\omega)|^2 \rangle} e^{-i\omega t} d\omega, \quad (3)$$

in which $H_a(\omega)$ is the response-corrected acceleration waveform computed from Hi-net records (equation 1). In both expressions (2) and (3), I use $\epsilon = 1\%$.

In Figure 4, the gray and black lines depict $D_{KK}(S,B,t)$ and $D_{KH}(S,B,t)$, respectively, obtained from the earthquake in Figure 1. Figure 4a shows the unfiltered waveforms, and Figure 4b shows the bandlimited (1–13 Hz) waveforms. These deconvolved waveforms are similar, and the correlation coefficients of these waveforms in the time interval are 0.990 (Fig. 4a) and 0.996 (Fig. 4b). Note that this similarity indicates that one can use Hi-net data for applying deconvolution interferometry. In Figure 4a, some discrepancies of the waveforms are caused by the differences of the receiver responses of KiK-net and Hi-net below 0.6 Hz and above 20 Hz (see Fig. 2).

Discussion of Dynamic Resolution

Dynamic resolution is one of the main differences between KiK-net and Hi-net sensors (Table 1). In this section,

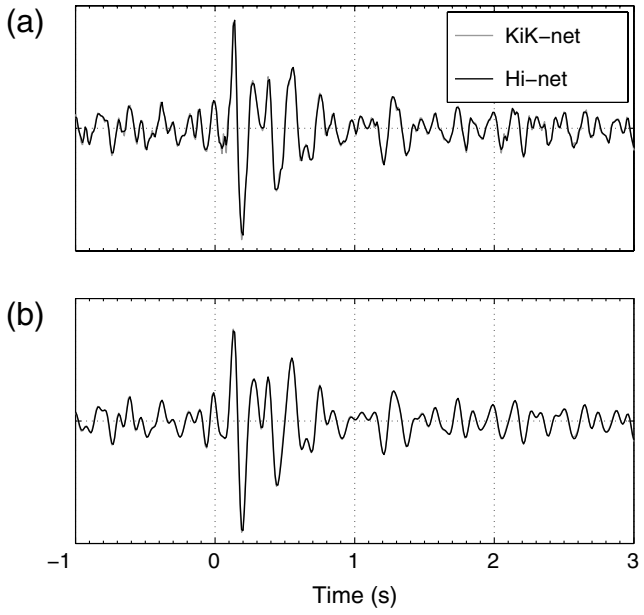

Figure 4. Comparison of deconvolved waveforms obtained from the earthquake shown in Figure 1 using only KiK-net records (gray line, equation 2) and the combination of KiK-net and Hi-net records (black line, equation 3). For the combination, I deconvolve the KiK-net record at the surface with the response-corrected Hi-net record at the borehole. Panel (a) is the unfiltered waveforms, and panel (b) the bandlimited (1–13 Hz) waveforms. Note that panel (b) also shows black and gray lines.

I use a numerical computation and show the influence of the dynamic resolution for deconvolved waveforms.

In the simplest case, where I assume vertically propagating waves between surface and borehole receivers, constant amplitude and wavenumber, and no internal reflections above the borehole receiver, I can represent the observed wavefields at the surface and borehole receivers as (Nakata and Snieder, 2012a)

$$u(S,\omega) = 2W(\omega)e^{ikR}e^{-\gamma|k|R} \tag{4}$$

$$u(B,\omega) = W(\omega)\{1 + e^{2ikR}e^{-2\gamma|k|R}\}, \tag{5}$$

in which $W(\omega)$ is the incoming wavefield to the borehole receiver, R is the distance between the surface and borehole receivers, k is the wavenumber, and γ is the attenuation coefficient. The incoming wavefield $W(\omega)$ may include complicated wave propagation (e.g., scattering and attenuation) below the borehole receiver. By applying deconvolution interferometry to these wavefields, in which I deconvolve $u(S,\omega)$ with $u(B,\omega)$, I can cancel $W(\omega)$, and the computed deconvolved waveform is independent of the complexity below the borehole receiver (Nakata and Snieder, 2012a).

I numerically compute expressions (4) and (5) with a 0.01 s time sampling, which is the same for KiK-net and Hi-net records (Table 1), and show the wavefields with the gray lines as the original waves in Figure 5a,b. For this numerical computation, I employ $R = 108$ m (which is the same as location N.HTAH), $W(\omega) = 1$ (delta function in the time domain) for simplicity, $\gamma = 1/60$, and the velocity of traveling waves is 750 m/s. The earthquake wave arrives at around 0.2 s at the borehole receiver.

To simulate KiK-net observed records (low-dynamic resolution; henceforth called the synthetic KiK-net record), I discretize the amplitudes of $u(S,t)$ in the 6.352×10^{-4} cm/s^2 interval and $u(B,t)$ in the 4.765×10^{-4} cm/s^2 interval, which correspond to the dynamic resolution of the KiK-net observation (Table 1). The black lines in Figure 5a,b show waveforms of the synthetic KiK-net records. To synthetically compute a Hi-net observed record (high-dynamic resolution; henceforth called synthetic Hi-net record), I first integrate $u(B,t)$ and discretize the amplitude of integrated waveforms in the 1.023×10^{-5} cm/s (Table 1). Then I differentiate the discretized waveform and create an acceleration waveform as the synthetic Hi-net record.

The black line in Figure 5c illustrates the deconvolved waveform computed by the synthetic KiK-net records at both surface and borehole receivers (simulated $D_{KK}(S,B,t)$). In Figure 5d, the black line depicts the waveform computed by the combination of the synthetic Hi-net (borehole) and KiK-net (surface) records (simulated $D_{KH}(S,B,t)$). I also show the deconvolved waveform obtained from the original waveform at the surface receiver and the synthetic KiK-net record at the borehole receiver (the black line in Figure 5e). The gray lines in Figure 5c–e illustrate the deconvolved waveform obtained from the original observed waveforms.

Although direct traveling waves (at around 0.14 s) are reconstructed with almost correct amplitudes and arrival times in Figure 5c–e, deconvolved waves at later times deviate from the original waveforms in Figure 5c,e. Waves after the direct arrival are multiply reflected waves between the free surface and the clamped boundary at the virtual source (Snieder *et al.*, 2006). One can also use these reflected waves for estimating wave velocities and attenuation of a medium (Nakata *et al.*, 2013). When I use the synthetic Hi-net record for the borehole wavefield, the deviations become small (compare the black and gray lines in Figure 5d). Therefore, I conclude that I obtain more correct deconvolved waveforms (more similar to the original deconvolved waveform in both phases and amplitudes) when I use Hi-net data for the borehole wavefield of the deconvolution interferometry. Comparing Figure 5d with Figure 5e, I discover that dynamic resolution in the denominator of the deconvolution in the frequency domain (borehole receiver) is more sensitive for deconvolved waves than that in the numerator (surface receiver).

Short-Time Moving-Window Seismic Interferometry

One advantage of using Hi-net records is that Hi-net data have the higher dynamic resolution than KiK-net data as discussed in the Discussion of Dynamic Resolution section. The other advantage is that Hi-net wavefields (velocity meter) have higher SNR than KiK-net records (accelerometer) (Clinton and Heaton, 2002). Here, I examine the advantage

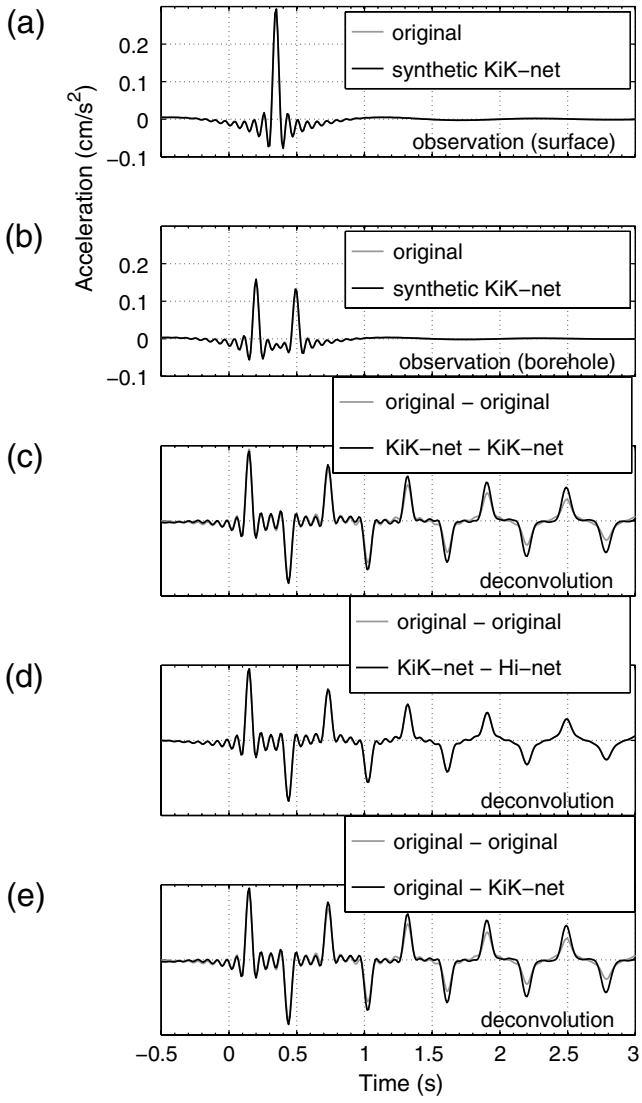

Figure 5. Synthetic observed waveforms recorded at the (a) surface and (b) borehole receivers. The gray and black lines show the original and synthetic KiK-net waveforms, respectively. (c) Deconvolved waveforms computed from the synthetic KiK-net records (simulated $D_{KK}(S,B,t)$). (d) Deconvolved waveforms computed from the synthetic KiK-net (surface) and Hi-net (borehole) records (simulated $D_{KH}(S,B,t)$). (e) Deconvolved waveforms computed from the original (surface) and the synthetic KiK-net (borehole) waveforms. The gray lines in panels (c)–(e) are deconvolved waveforms computed from the original waveforms for both surface and borehole receivers. The waveforms are filtered for the same band used in Figure 4b.

of the SNR using short-time moving-window seismic interferometry (SMSI). Nakata and Snieder (2011) found a nonlinear response caused by the 2011 Tohoku-Oki earthquake using SMSI. Because for SMSI we compute deconvolution in a short time segment, this technique is more sensitive to SNR than normal deconvolution interferometry using entire earthquake records as shown in Figure 4.

Figure 6 shows the SMSI waveforms obtained from the earthquake used in Figure 1. In Figure 6, I compute deconvolution of the waveforms at each 20 s time interval with a 10 s overlap for SMSI. Using KiK-net records only (Fig. 6c), I reconstruct the traveling waves, which have prominent peaks at around 0.14 s, from the data during 0–60 s (first seven deconvolved waveforms). The last three waveforms (70–110 s) are noisy and have no coherent peaks at 0.14 s. In contrast, when I use both Hi-net and KiK-net data (Fig. 6d), I obtain the deconvolved waveforms with explicit peaks throughout the time intervals. For example comparing the waveforms of the interval of 90–110 s, the peak of the waveform at 0.14 s in Figure 6d is clearer than that in Figure 6c. The coherent waves at around 0.5 s in Figure 6d are the first-order surface-related multiple waves, which reflect between the free surface and the clamped boundary at the virtual source.

Figure 6e shows lag times of the maximum amplitude for each deconvolved wave in Figure 6c,d. Usually, the time of the maximum amplitude relates to the arrival time of direct traveling waves from the borehole receiver to the surface sensor (see Fig. 5). Therefore in Figure 6e, when the lag times deviate from the dashed line, we have the potential for estimating an incorrect arrival time. Because nine time intervals show correct arrival times in black but only four intervals in gray in Figure 6e, I improve the quality of the estimated arrival times using Hi-net records. Here, the correct arrival time is defined as the time represented by the dashed line in Figure 6e ± 0.01 s because I do not know the exact arrival time. I can also improve the quality of the estimated shear-wave splitting (Nakata and Snieder, 2012a) by applying this technique to two horizontal components.

Figure 6b shows SNR computed by the root mean square (rms) amplitude at each time interval of the earthquake record used in Figure 6 and an rms amplitude of background noise. To obtain a stable rms amplitude of background noise, I use approximately 100 earthquake records and look at the time intervals before *P* waves arrive. Figure 6b indicates that Hi-net data have higher SNR than KiK-net data at all time intervals, which is the main reason for the highly coherent deconvolved waveforms among different time intervals in Figure 6d.

Using Hi-net data, I obtain clear traveling wavefields even at later observed times due to the higher SNR. This advantage of the SNR is also important for deconvolved waveforms computed from coda waves (Sawazaki *et al.*, 2009; Takagi and Okada, 2012) because the amplitudes of coda waves are usually smaller than those of direct waves, and the SNR at the time of coda waves is small. Deconvolved waveforms of SMSI using the other earthquake and station are shown in Figures A3 and A4, which also show improved coherence of the waveforms using the combination of Hi-net and KiK-net data.

Conclusion

I propose the technique of using both Hi-net and KiK-net data for deconvolution interferometry. In this technique, I use Hi-net data as a borehole record and KiK-net data as a

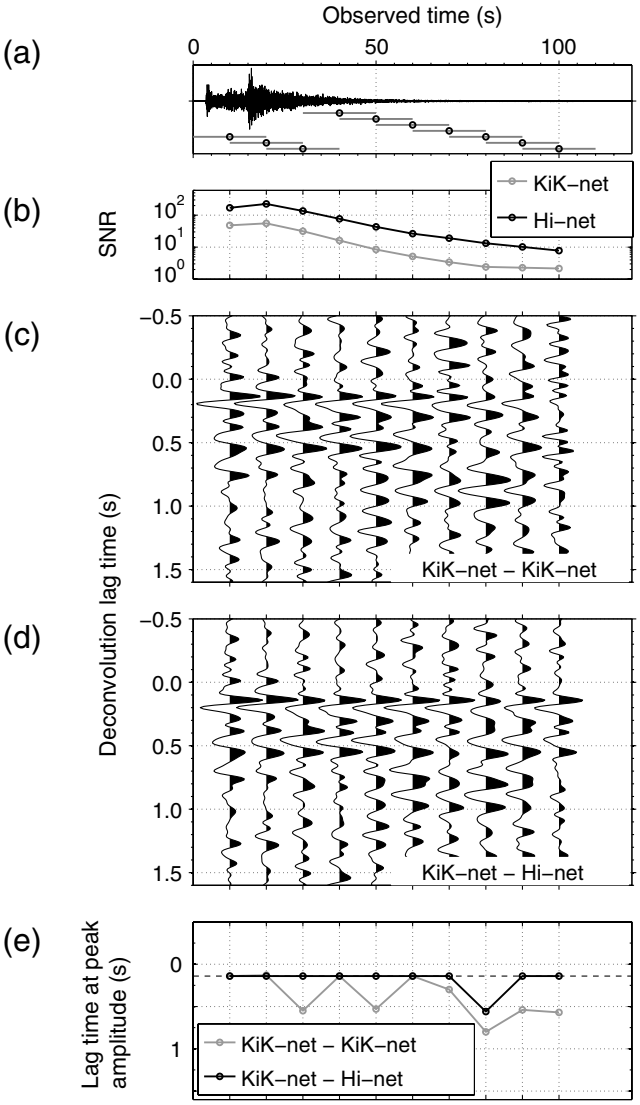

Figure 6. (a) Observed waveforms recorded at the KiK-net borehole receiver (the same waveforms shown in Figure 1e). Gray lines indicate the 20 s time windows for SMSI with a 10 s overlap. Black circles represent the center of each time window. (b) SNR of KiK-net (gray) and response-corrected Hi-net records (black) computed from the rms amplitude at each time interval divided by the rms amplitude of background noise. (c) Deconvolved waveforms at each time interval using only KiK-net records. (d) Deconvolved waveforms computed from the combination of KiK-net (surface) and Hi-net (borehole) records. (e) Lag times of the peak amplitude at each deconvolved waveform in panel (c) in gray and panel (d) in black. The dashed horizontal line shows the arrival time of the direct traveling wave estimated by Nakata and Snieder (2012a). Waveforms in panels (c) and (d) are filtered for the same band used in Figure 4b. Waveforms and circles in panels (b)–(e) are aligned with the center time of the time windows shown in panel (a).

surface record to compute deconvolution. Because of the difference in receiver responses of Hi-net and KiK-net, I need to correct the response of the Hi-net records. After the correction, the waveform of Hi-net is similar to that of KiK-net especially in the frequency range used in this study (1–13 Hz). The deconvolved waveforms obtained from entire earthquake records using the combination of Hi-net and KiK-net receivers are similar to those using only KiK-net sensors, which indicates that I can use Hi-net data for computing deconvolution. Because Hi-net wavefields have high SNR and high dynamic resolution, deconvolved waveforms computed by the combination have two advantages over the conventional deconvolved waveforms obtained by using only KiK-net data: higher SNR and better amplitude and phase information. These advantages are important for SMSI and deconvolution interferometry using coda waves. Note that Hi-net receivers are already installed at all of the KiK-net sites, and this technique uses existing data to improve deconvolution interferometry.

Data and Resources

KiK-net and Hi-net data are operated and maintained by the NIED. Frequency responses of the Hi-net observation equipment are shown at http://www.hinet.bosai.go.jp/REGS/seed/ (last accessed July 2013).

Acknowledgments

This study is supported by the Consortium Project on Seismic Inverse Methods for Complex Structures at the Center for Wave Phenomena. I am grateful to Roel Snieder of Colorado School of Mines for his advice to improve this study. I also thank Shoichi Masuhara for his technical help, Marine Denolle of Stanford University for her insight and beneficial discussions to start this study, and Associate Editor Eric Chael and anonymous reviewers for suggestions and comments.

References

Aoi, S., T. Kunugi, and H. Fujiwara (2004). Strong-motion seismograph network operated by NIED: K-NET and KiK-net, *J. Japan Assoc. Earthq. Eng.* **4,** 65–74.

Aoi, S., T. Kunugi, H. Nakamura, and H. Fujiwara (2011). Deployment of new strong motion seismographs of K-NET and KiK-net, earthquake data in engineering seismology, *Geotech. Geol. Earthq. Eng.* **14,** 167–186.

Clayton, R. W., and R. A. Wiggins (1976). Source shape estimation and deconvolution of teleseismic bodywaves, *Geophys. J. Roy. Astron. Soc.* **47,** 151–177.

Clinton, J. F., and T. H. Heaton (2002). Potential advantages of a strong-motion velocity meter over a strong-motion accelerometer, *Seismol. Res. Lett.* **73,** no. 3, 332–342.

Havskov, J., and L. Ottemöller (2010). *Routine Data Processing in Earthquake Seismology with Sample Data, Exercises and Software*, Springer, Netherlands, 347 pp.

Héloïse, C., P.-Y. Bard, and A. Rodriguez-Marek (2012). Site effect assessment using KiK-net data: Part 1. A simple correction procedure for surface/downhole spectral ratios, *Bull. Earthq. Eng.* **10,** 421–448.

Minato, S., T. Tsuji, S. Ohmi, and T. Matsuoka (2012). Monitoring seismic velocity change caused by the 2011 Tohoku-oki earthquake using ambient noise records, *Geophys. Res. Lett.* **39,** no. L09309, doi: 10.1029/2012GL051405.

Nakata, N., and R. Snieder (2011). Near-surface weakening in Japan after the 2011 Tohoku-Oki earthquake, *Geophys. Res. Lett.* **38,** no. L17302, doi: 10.1029/2011GL048800.

Nakata, N., and R. Snieder (2012a). Estimating near-surface shear-wave velocities in Japan by applying seismic interferometry to KiK-net data, *J. Geophys. Res.* **117,** no. B01308, doi: 10.1029/2011JB008595.

Nakata, N., and R. Snieder (2012b). Time-lapse change in anisotropy in Japan's near surface after the 2011 Tohoku-Oki earthquake, *Geophys. Res. Lett.* **39,** no. L11313, doi: 10.1029/2012GL051979.

Nakata, N., R. Snieder, S. Kuroda, S. Ito, T. Aizawa, and T. Kunimi (2013). Monitoring a building using deconvolution interferometry. I: Earthquake-data analysis, *Bull. Seismol. Soc. Am.* **103,** no. 3, 1662–1678, doi: 10.1785/0120120291.

Obara, K., K. Kasahara, S. Hori, and Y. Okada (2005). A densely distributed high-sensitivity seismograph network in Japan: Hi-net by National Research Institute for Earth Science and Disaster Prevention, *Rev. Sci. Instrum.* **76,** 021,301, doi: 10.1063/1.1854197.

Okada, Y., K. Kasahara, S. Hori, K. Obara, S. Sekiguchi, H. Fujiwara, and A. Yamamoto (2004). Recent progress of seismic observation networks in Japan—Hi-net, F-net, K-NET and KiK-net, *Earth Planets Space* **56,** 15–28.

Sawazaki, K., and R. Snieder (2013). Time-lapse changes of *P*- and *S*-wave velocities and shear wave splitting in the first year after the 2011 Tohoku earthquake, Japan: Shallow subsurface, *Geophys. J. Int.* **193,** 238–251.

Sawazaki, K., H. Sato, H. Nakahara, and T. Nishimura (2006). Temporal change in site response caused by earthquake strong motion as revealed from coda spectral ratio measurement, *Geophys. Res. Lett.* **33,** L21,303, doi: 10.1029/2006GL027938.

Sawazaki, K., H. Sato, H. Nakahara, and T. Nishimura (2009). Time-lapse changes of seismic velocity in the shallow ground caused by strong ground motion shock of the 2000 western-Tottori earthquake, Japan, as revealed from coda deconvolution analysis, *Bull. Seismol. Soc. Am.* **99,** no. 1, 352–366.

Shiomi, K., K. Obara, S. Aoi, and K. Kasahara (2003). Estimation on the azimuth of the Hi-net and KiK-net borehole seismometers, *Zishin 2* (in Japanese), **56,** 99–110.

Shiomi, K., K. Obara, and K. Kasahara (2005). Amplitude saturation of the NIED Hi-net waveforms and simple criteria for recognition, *Zishin 2* (in Japanese), **57,** 451–461.

Snieder, R., J. Sheiman, and R. Calvert (2006). Equivalence of the virtual-source method and wave-field deconvolution in seismic interferometry, *Phys. Rev. E* **73,** 066,620, doi: 10.1103/PhysRevE.73.066620.

Takagi, R., and T. Okada (2012). Temporal change in shear velocity and polarization anisotropy related to the 2011 *M* 9.0 Tohoku-Oki earthquake examined using KiK-net vertical array data, *Geophys. Res. Lett.* **39,** no. L09310, doi: 10.1029/2012GL051342.

Wegler, U., H. Nakahara, C. Sens-Schönfelder, M. Korn, and K. Shiomi (2009). Sudden drop of seismic velocity after the 2004 M_w 6.6 mid-Niigata earthquake, Japan, observed with passive image interferometry, *J. Geophys. Res.* **114,** no. B06305, doi: 10.1029/2008JB005869.

Wu, C., and Z. Peng (2011). Temporal changes of site response during the 2011 M_w 9.0 off the Pacific coast of Tohoku Earthquake, *Earth Planets Space* **63,** 1–5.

Wu, C., and Z. Peng (2012). Long-term change of site response after the M_w Tohoku earthquake in Japan, *Earth Planets Space* **64,** 1259–1266.

Yamada, M., J. Mori, and S. Ohmi (2010). Temporal changes of subsurface velocities during strong shaking as seen from seismic interferometry, *J. Geophys. Res.* **115,** no. B03302, doi: 10.1029/2009JB006567.

Appendix A

Examples of Another Earthquake and Station

In this Appendix, I show the comparison of wavefields observed by Hi-net and KiK-net in the frequency domain (Figs. A1 and A2) and deconvolved waveforms after applying SMSI (Figs. A3 and A4) obtained from other earthquakes recorded at the same station (N.HTAH and FKSH12) and another station, which is in the Hyogo prefecture (Hi-net code: N.SNTH, KiK-net code: HYGH11). Based on Figures A1–A4, the technique proposed in this study is valid for other earthquakes and stations.

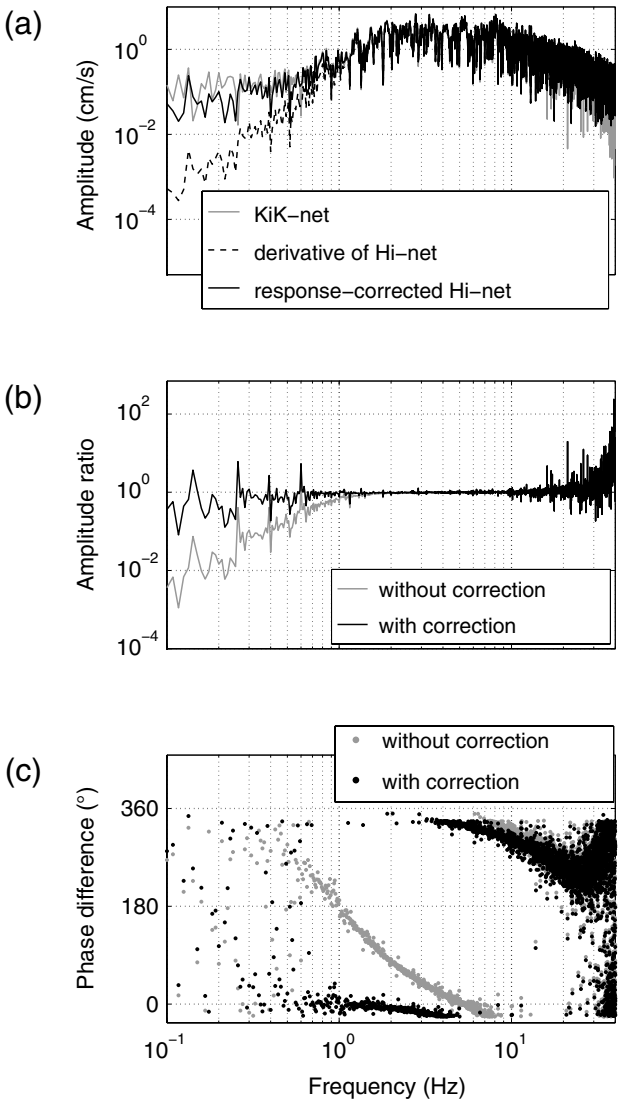

Figure A1. (a) Comparison of amplitude spectra computed from waveforms generated by an earthquake, which occurred at 21:48:43, 4 January 2012 (JST). The epicenter is at 36.574° N and 141.148° N, and the depth is 32.9 km. The station is the same as used in Figure 2 (N.HTAH and FKSH12). The gray line illustrates the amplitude spectra of the KiK-net borehole record, the dashed black line indicates the derivative of the Hi-net record, and the solid black line shows the response-corrected Hi-net record. (b) Ratios of amplitude spectra (Hi-net/KiK-net). The gray line is computed from the amplitude spectra shown in the gray and dashed black lines in panel (a), and the black line from the gray and solid black lines in panel (a). (c) Differences of phase spectra (Hi-net–KiK-net). The gray and black dots are computed from the waveforms used for the gray and black lines in panel (b). Because of the display, some dots are shown around 360°.

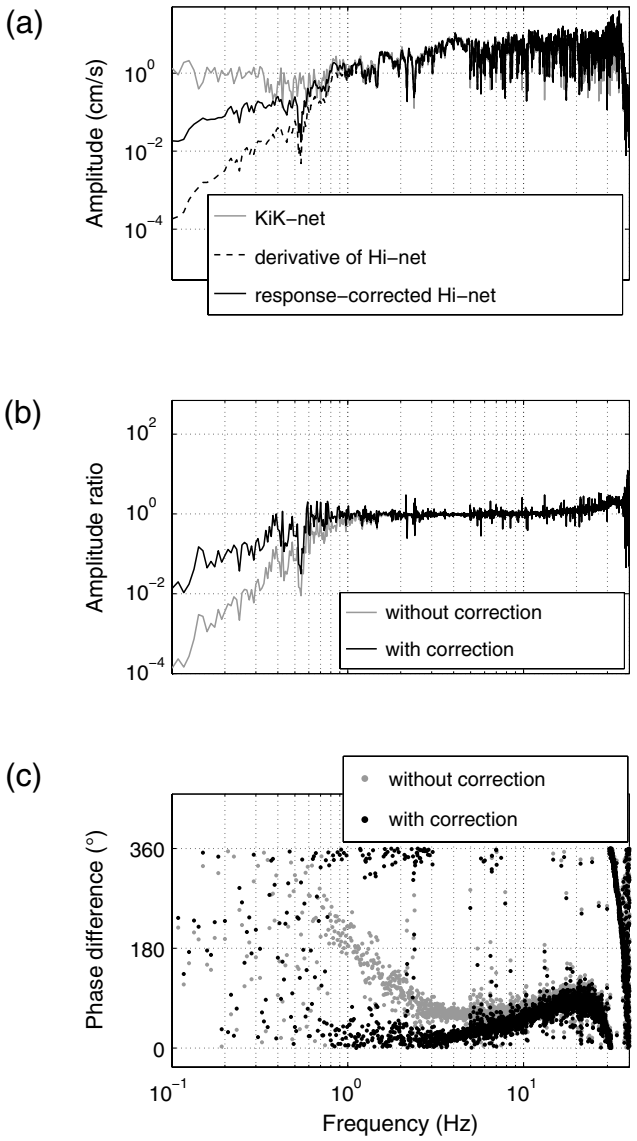

Figure A2. (a) Comparison of amplitude spectra computed from waveforms generated by an earthquake, which occurred at 21:45:24, 12 July 2004 (JST). The epicenter is at 34.970° N and 134.676° E, and the depth is 10.4 km. The station is in the Hyogo prefecture (N.SNTH and HYGH11). The gray line illustrates the amplitude spectra of the KiK-net borehole record, the dashed black line shows the derivative of the Hi-net record, and the solid black line indicates the response-corrected Hi-net record. (b) Ratios of amplitude spectra (Hi-net/KiK-net). The gray line is computed from the amplitude spectra shown in the gray and dashed black lines in panel (a), and the black line from the gray and solid black lines in panel (a). (c) Differences of phase spectra (Hi-net–KiK-net). The gray and black dots are computed from the waveforms used for the gray and black lines in panel (b). Because of the display, some dots are shown around 360°.

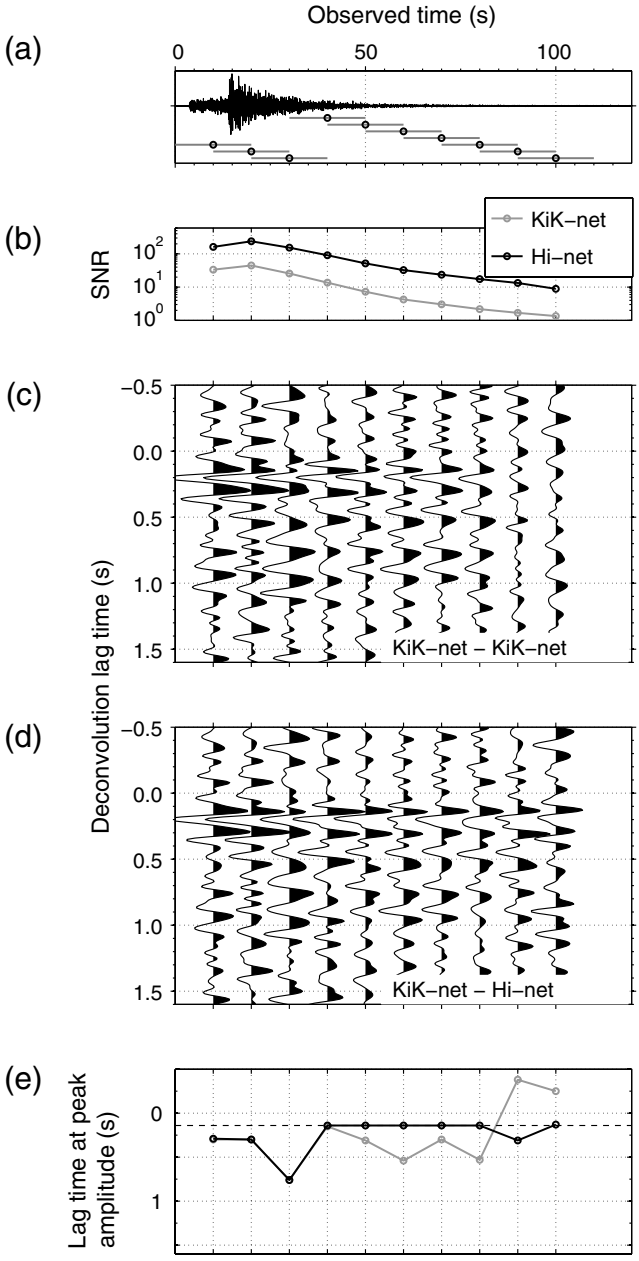

Figure A3. (a) Observed waveforms recorded at the KiK-net borehole receiver obtained from the earthquake used in Figure A1. Gray lines indicate the 20 s time windows for SMSI with a 10 s overlap. Black circles represent the center of each time window. (b) SNR of KiK-net (gray) and response-corrected Hi-net records (black) computed by the rms amplitude at each time interval divided by the rms amplitude of background noise. (c) Deconvolved waveforms at each time interval using only KiK-net records. (d) Deconvolved waveforms computed from the combination of KiK-net (surface) and Hi-net (borehole) records. (e) Lag times of the peak amplitude at each deconvolved waveform in panel (c) in gray and panel (d) in black. The dashed horizontal line shows the arrival time of the direct traveling wave estimated by Nakata and Snieder (2012a). Waveforms in panels (c) and (d) are filtered for the same band used in Figure 4b. Waveforms and circles in panels (b)–(e) are aligned with the center time of the time windows shown in panel (a).

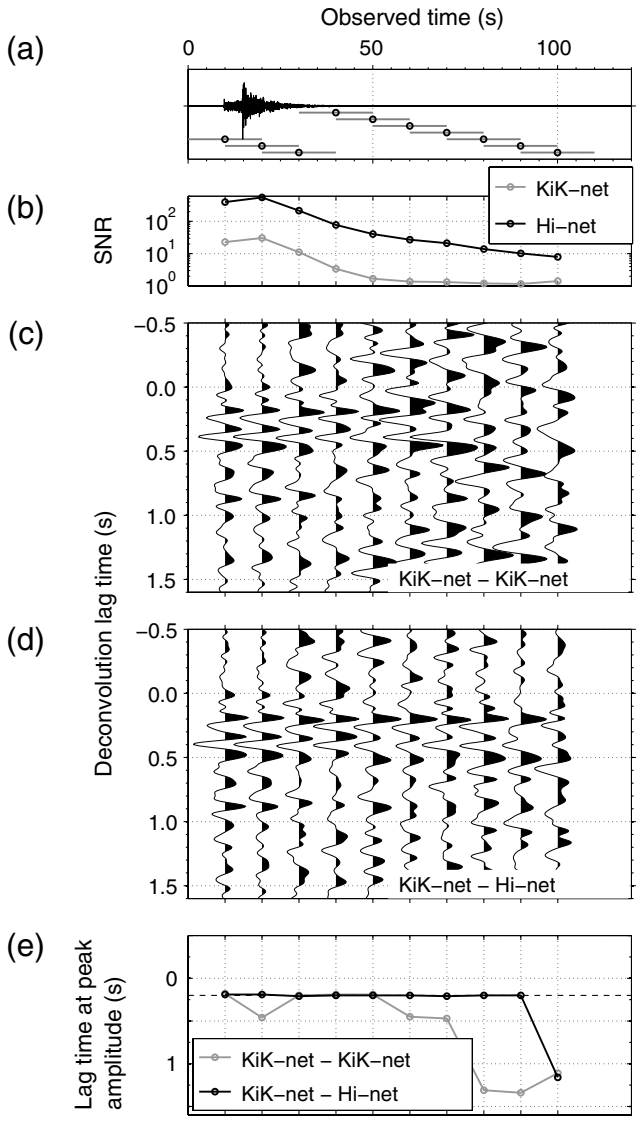

Figure A4. (a) Observed waveforms recorded at the KiK-net borehole receiver obtained from the earthquake used in Figure A2. Gray lines indicate the 20 s time windows for SMSI with a 10 s overlap. Black circles represent the center of each time window. (b) SNR of KiK-net (gray) and receiver-response corrected Hi-net records (black) computed by the rms amplitude at each time interval divided by the rms amplitude of background noise. (c) Deconvolved waveforms at each time interval using only KiK-net records. (d) Deconvolved waveforms computed from the combination of KiK-net (surface) and Hi-net (borehole) records. (e) Lag times of the peak amplitude at each deconvolved waveform in panel (c) in gray and panel (d) in black. The dashed horizontal line shows the arrival time of the direct traveling wave estimated by Nakata and Snieder (2012a). Waveforms in panels (c) and (d) are filtered for the same band used in Figure 4b. Waveforms and circles in panels (b)–(e) are aligned with the center time of the time windows shown in panel (a).

Department of Geophysics
Stanford University
397 Panama Mall
Stanford, California 94305
nnakata@stanford.edu

Manuscript received 25 April 2013;
Published Online 5 November 2013